The HBx protein from hepatitis B virus coordinates a redox-active Fe-S cluster

Chie Ueda , Michelle Langton , Jiahua Chen, and Maria-Eirini Pandelia*
From the Department of Biochemistry, Brandeis University, Waltham, Massachusetts, USA

Edited by Ruma Banerjee

The viral protein HBx is the key regulatory factor of the hepatitis B virus (HBV) and the main etiology for HBV-associated liver diseases, such as cirrhosis and hepatocellular carcinoma. Historically, HBx has defied biochemical and structural characterization, deterring efforts to understand its molecular mechanisms. Here we show that soluble HBx fused to solubility tags copurifies with either a [2Fe-2S] or a [4Fe-4S] cluster, a feature that is shared among five HBV genotypes. We show that the O_2-stable [2Fe-2S] cluster form converts to an O_2-sensitive [4Fe-4S] state when reacted with chemical reductants, a transformation that is best described by a reductive coupling mechanism reminiscent of Fe-S cluster scaffold proteins. In addition, the Fe-S cluster conversions are partially reversible in successive reduction–oxidation cycles, with cluster loss mainly occurring during (re)oxidation. The considerably negative reduction potential of the $[4Fe-4S]^{2+/1+}$ couple (−520 mV) suggests that electron transfer may not be likely in the cell. Collectively, our findings identify HBx as an Fe-S protein with striking similarities to Fe-S scaffold proteins both in cluster type and reductive transformation. An Fe-S cluster in HBx offers new insights into its previously unknown molecular properties and sets the stage for deciphering the roles of HBx-associated iron (mis)regulation and reactive oxygen species in the context of liver tumorigenesis.

Chronic hepatitis B virus (HBV) infection affects 300 million people globally and is a major risk factor for the development of hepatocellular carcinoma (1, 2). HBV is classified into 10 genotypes that appear in distinct geographical locations and are associated with different clinical outcomes or disease severity (3, 4). All HBV genotypes share a common genomic architecture featuring four overlapping genes (*P*, *S*, *C*, and *X*) encoding for seven viral proteins (5). Protein X (or HBx) is required for viral replication and is a key factor in chronic HBV-related hepatocarcinogenesis (6–8). HBx promotes transcription of the extrachromosomal HBV genome by hijacking the DNA-damage binding protein 1 (DDB1)-containing E3 ubiquitin ligase to target the "structural maintenance of chromosomes" (Smc) Smc5/6 complex for degradation (9). This mechanism stimulates transcription of episomal DNA templates as well as the HBV genome, giving HBx the title of a transcriptional transactivator (10). HBx has also been shown to promote viral replication by recruiting Parvulin 14 and 17 to the HBV covalently closed circular DNA to enhance transcriptional activation (11). In addition, HBx is reported to affect many oncogenic-related cellular processes, such as cell proliferation, DNA damage repair, and Fe regulation (12). For example, HBx has been linked to altered iron metabolism and iron regulatory protein 1 (IRP1) expression in hepatic cells, and is suggested to inhibit the tumor suppressor PTEN via the production of reactive oxygen species (ROS) (13, 14). Most of our current understanding of HBx is inferred from cellular experiments (reviewed in detail in the following refs: (12, 15, 16)), and thus the molecular mechanisms that underlie HBx activity remain obscure.

HBx is a small 154 amino acid protein with a cysteine-rich sequence that is highly conserved across the various HBV genotypes. Naturally occurring C-terminally truncated (30–40 aa) or N-terminally elongated (52 aa) forms of HBx are associated with different disease outcomes (17, 18). Although both canonical and noncanonical HBx proteins share pronounced sequence identity, the lack of sequence similarity to any known proteins hinders inference of molecular structure and function. The historically poor solution behavior of HBx has confined *in vitro* studies to samples that are nonnative, highly truncated, or contain extensive amino acid substitutions, often leading to conflicting outcomes and inadequate biophysical and biochemical characterization (19–21). Solubility enhancement tags have successfully provided a first insight into the molecular properties of HBx, especially in its metal binding potential. HBx fused to the Maltose Binding Protein (MBP-HBx) copurifies with significant amounts of Fe and Zn (20) and was recently assigned as a Zn-binding protein based on the copurification of Zn when coexpressed or fused to DDB1 (22). C61, C69, C137, and H139 were identified as potential ligands to the Zn cofactor, and the residues of this CCCH motif were shown to be critical for HBx viral replication function (*i.e.*, targeting the Smc5/6 complex for degradation). However, there was no evidence that Zn binding facilitates protein–protein interactions with DDB1, leaving the functional role of Zn binding in HBx unresolved.

In the present study, we focus on a soluble construct of HBx fused to disulfide bond isomerase C (DsbC-HBx) (23) to delve into the potential of HBx to coordinate transition metal ions.

* For correspondence: Maria-Eirini Pandelia, mepandelia@brandeis.edu.

HBx from HBV coordinates an Fe-S cluster

We find that HBx copurifies with Fe assembled into an Fe-S cluster, establishing HBx as an unrecognized Fe-S protein. HBx binds two different types of Fe-S clusters: a [2Fe-2S] or [4Fe-4S] cluster depending on the presence or absence of oxygen, respectively. Through multiple spectroscopic approaches, we characterize the chemical nature and redox attributes of the newfound Fe-S cluster in HBx. Interestingly, the [2Fe-2S] cluster form undergoes a reductive rearrangement that affords formation of [4Fe-4S] clusters. This transformation is best described by a reductive coupling mechanism that is a well-studied and characteristic feature of Fe-S cluster scaffold proteins, such as IscU and IscA. This parallel is intriguing and invokes the notion that HBx may potentially hijack cellular pathways by affecting Fe-S cluster biogenesis (24). Despite this similarity, however, there are multiple ways by which the Fe-S cluster in HBx may be important either at a structural or a regulatory level. Fe-S clusters are functionally diverse and ubiquitous cofactors that are becoming increasingly recognized as key components in viral proteins from rotaviruses, polyomaviruses, and more recently coronaviruses (25–29). The roles of Fe-S cofactors in viral proteins are proposed to be structural with critical outcomes in the host protein activity. In our study, the presence of the newfound Fe-S cluster sets the stage for interrogating the molecular and structural underpinnings of HBx, whereas its redox-dependent behavior outlines possible roles of the Fe-S cluster-bound HBx in Fe homeostasis.

Results

HBx is an Fe-S cluster–binding protein

Aerobically isolated DsbC- or MBP-HBx copurifies with 2.4 to 2.5 mol Fe per mol protein (Table S1). Both proteins exhibit a reddish brown color and optical features at 325, 415, and 460 nm, suggestive of the presence of a [2Fe-2S] cluster (30) (Fig. 1A). ^{57}Fe-enriched samples were examined by Mössbauer spectroscopy to confirm the exact chemical nature of the bound Fe species. The 4.2 K Mössbauer spectrum of the aerobically isolated DsbC-HBx was collected in a small magnetic field (78 mT) applied parallel to the direction of the γ irradiation (Fig. 1B) and shows a quadrupole doublet with parameters characteristic of antiferromagnetically coupled all-ferric [2Fe-2S]$^{2+}$ clusters (δ = 0.28 mm/s, ΔE_Q = 0.51 mm/s, ~84% of the total Fe absorption) (Table S2) (31, 32). A broad baseline spectrum makes up the rest of the signal intensity (16%) and is attributed to adventitiously bound high-spin (S = 5/2) Fe^{3+}. The Mössbauer spectrum of the aerobically isolated MBP-HBx is essentially identical to that of DsbC-HBx (Fig. 1C). Elemental analyses in tandem with Mössbauer spectroscopy indicate binding of one [2Fe-2S] cluster per polypeptide. Exact Fe-S cluster stoichiometry cannot be unequivocally determined because both fusion constructs purify as poorly defined higher-order oligomers as previously reported (20). The observed aggregation is partially due to intermolecular disulfides (Fig. S1) and unknown interactions that are salt and concentration independent.
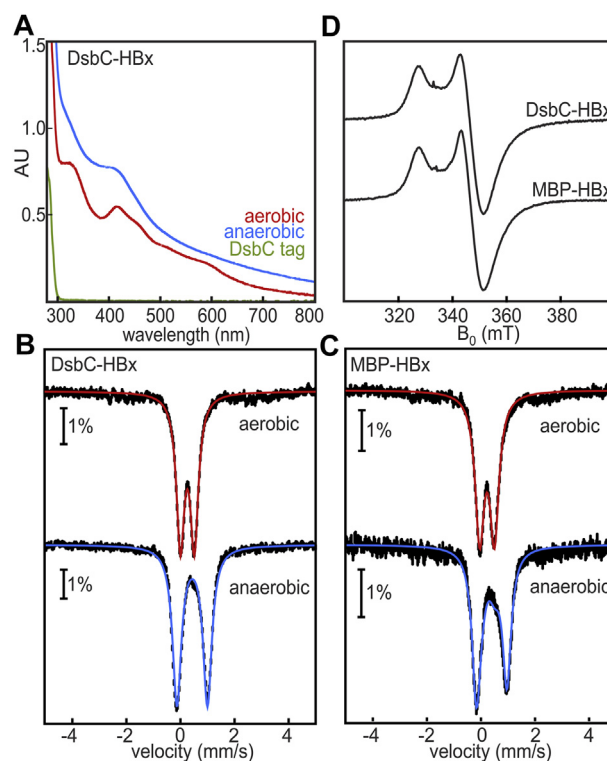

Figure 1. HBx is an Fe-S-binding protein. A, UV-visible spectra of DsbC-HBx isolated aerobically (*red line*) and anaerobically (*blue line*). DsbC (*green line*) shows no spectral features. B, Mössbauer spectra of DsbC-HBx aerobically (*top*) and anaerobically (*bottom*) isolated. C, Mössbauer spectra of MBP-HBx aerobically (*top*) and anaerobically (*bottom*) isolated. Mössbauer spectra were recorded at 4.2 K with a magnetic field (B = 78 mT) applied parallel to the γ-beam. D, X-band continuous wave (cw) EPR spectra of dithionite-reduced DsbC-HBx and MBP-HBx (microwave frequency = 9.38 GHz, T = 10 K, microwave power = 0.64 mW, modulation amplitude = 1 mT).

The HBx fusion proteins were also isolated under O$_2$-free conditions to examine whether the [2Fe-2S] cluster arises from oxidative degradation of a more O$_2$-sensitive [4Fe-4S] cluster form. The UV-visible spectrum of the anaerobically purified DsbC-HBx exhibits a band at 420 nm, consistent with the presence of [4Fe-4S] clusters (Fig. 1A) (30). The 4.2 K/78 mT Mössbauer spectrum of the anaerobically purified DsbC-HBx is dominated by a single quadrupole doublet with δ = 0.45 mm/s and ΔE_Q = 1.11 mm/s (Fig. 1B), confirming the presence of [4Fe-4S]$^{2+}$ clusters and supporting the hypothesis that the [2Fe-2S] clusters detected in the aerobically isolated protein are oxidative products. The anaerobically purified MBP-HBx has a similar spectrum with the [4Fe-4S]$^{2+}$ cluster as the major component (60% of total Fe absorption). The remaining absorption can be ascribed to a subspectrum of [2Fe-2S]$^{2+}$ clusters (~17%), and a broad paramagnetic subspectrum assigned to Fe polysulfides formed during the purification process (~23%) (Fig. 1C). Parallel experiments on whole *Escherichia (E.) coli* cells monitored by Mössbauer spectroscopy showed that the [2Fe-2S] cluster form is also present in whole cells (Fig. S2), suggesting that [2Fe-2S] clusters in HBx may be both an oxidative outcome and a consequence of incomplete Fe-S cluster insertion due to overexpression in *E. coli*. There is no evidence for formation of

$[3Fe-4S]^{1+}$ clusters in the aerobically purified protein, as demonstrated by electron paramagnetic resonance (EPR) (Fig. S3); therefore, the $[2Fe-2S]^{2+}$ form appears to be the only stable oxidative by-product of the [4Fe-4S] cluster form.

Dithionite reduction of the aerobically isolated DsbC- and MBP-HBx yields EPR spectra with identical parameters and lineshape irrespective of the solubility tag (Fig. 1D). The observed signals have axial symmetry, principal g-values of 2.04, 1.94, and 1.94, and relaxation properties that are best attributed to $S = 1/2$ $[4Fe-4S]^{1+}$ clusters rather than $[2Fe-2S]^{1+}$ clusters (Figs. 1D and S4). These data suggest that reductive treatment generates $[4Fe-4S]^{1+}$ clusters, possibly as a result of reductive coupling (*vide infra*). This process, which has been observed in Fe-S cluster chaperone proteins and proteins that act as Fe-S cluster donors, involves the one-electron reduction of $[2Fe-2S]^{2+}$ to $[2Fe-2S]^{1+}$ clusters, followed by the coupling of two $[2Fe-2S]^{1+}$ clusters to form one $[4Fe-4S]^{2+}$ cluster. Cleavage of the DsbC tag by tobacco etch virus protease does not result in Fe-S cluster loss (as seen by EPR, Fig. S5); however, we were unable to separate out the DsbC tag.

Fe-S cluster binding is a common feature of HBx across different genotypes

Bioinformatic analyses identified ∼6800 HBx sequences that share a high degree of sequence identity (>80%). HBx sequences are rich in cysteines, seven of which are invariant (Fig. 2A). Because Fe-S cluster binding is primarily cysteine dependent, we suspect that some of these conserved cysteines are involved in cofactor binding in HBx. Other residues, such as histidine, aspartate, and arginine can also contribute to Fe-S cluster coordination (33). In this respect, the strictly conserved H139 may also serve as a ligand. Single substitution of each of the conserved cysteines (Fig. 2A) with alanine did not affect Fe-S incorporation, and only a variant lacking all cysteines was unable to coordinate an Fe-S cluster (Fig. S6). We also identified a highly conserved leucine–tyrosine–arginine (LYR)-like motif in the HBx primary sequence (Fig. 2A). Such a motif has been shown to be a recognition sequence for direct interaction with the Fe-S cochaperone HSC20 (34), which may further support the fact that HBx can receive an Fe-S cluster from the biosynthetic machinery.

Although the sequence similarity network (SSN) maps little segregation due to high sequence identity, it is overall clustered by the extant HBV genotype. HBx from the HBV genotypes A, C, and D (shown in red, orange, and green, respectively, Fig. 2B) exhibit the highest sequence homology to each other. Genotypes A and D are distributed pandemically in populations worldwide, whereas genotype C is found primarily in East Asia (3, 4). From genotype C we selected a sequence designated "whole-HBx" or wHBx, which includes an N-terminal 52-aa extension, to increase sequence variability. The two most sequence-diverse genotypes that cluster separately in the SSN (*i.e.*, B and F1) are mainly found in East Asia and South America, respectively (3, 4). On the basis of their distribution and clinical importance, DsbC fusions were generated with select sequences from the A2, B, C, D, and F1 HBV

genotypes. All five proteins were ^{57}Fe-enriched for characterization by Mössbauer spectroscopy and isolated under O_2-free conditions. The isolated DsbC-HBx fusions all coordinate both $[2Fe-2S]^{2+}$ and $[4Fe-4S]^{2+}$ clusters (Fig. 2C), albeit at different relative ratios (Table S3), demonstrating that Fe-S cluster binding is a common feature across diverse HBx sequences.

Zn may substitute for the Fe-S cluster in HBx

DsbC-HBx was expressed in LB media supplemented with Fe and Zn salts to examine the extent of cofactor incorporation on the basis of metal availability. Cells overexpressing DsbC-HBx exhibit a light brown color, indicating enrichment in Fe-S clusters, whereas cells overexpressing DsbC alone lack color (Fig. 3A). Therefore, cell pellet color is an initial indicator for Fe-S cluster incorporation under different metal supplementation conditions. Supplementation with 250 μM $ZnSO_4$ causes a lighter-colored pellet, whereas, supplementation with 250 μM $Fe(NH_4)_2(SO_4)_2$ results in a dark brown pellet (Fig. 3A). DsbC-HBx expression with simultaneous Zn and Fe supplementation leads to brown cell pellets that are lighter colored than those obtained from cells supplemented with Fe alone, suggesting that Zn may partially inhibit Fe incorporation when added in equimolar amounts. SDS-PAGE analysis of normalized cell pellets shows a similar expression level of the ∼42-kDa DsbC-HBx in the LB, LB(Fe), LB(Zn), and LB(Fe,Zn) cells (Fig. 3B). The optical spectra of the aerobically purified proteins show formation of a $[2Fe-2S]^{2+}$ cluster under all conditions, but signal intensity is decreased when Zn is added to the media, consistent with compromised Fe-S incorporation (Fig. 3, C and D). These results highlight that (i) Zn competes with the Fe-S cluster for binding to HBx, suggestive of a common coordination site, and (ii) Fe-S cofactor assembly is favored over Zn incorporation supporting that the Fe-S cluster may be the preferred cofactor *in cellulo*.

The [4Fe-4S] cluster in HBx may be formed by reductive coupling of two [2Fe-2S] clusters

Stoichiometric reduction

The aerobically purified DsbC-HBx coordinates 1.0 [2Fe-2S] cluster per protein (Figs. 4 and S7) and some adventitiously bound high-spin Fe^{3+}, which is inaccessible to chelating agents. The observed formation of $[4Fe-4S]^{1+}$ clusters by dithionite reduction of DsbC-HBx:[2Fe-2S] in EPR (Fig. 1D) prompted us to examine this process in more detail by ^{57}Fe Mössbauer spectroscopy. The [2Fe-2S] to [4Fe-4S] cluster transformation requires a strong reducing agent (*i.e.*, sodium dithionite) and is not induced by weaker thiol-based reductants such as DTT or by the *Azotobacter (A.) vinelandii iscFdx* (Fig. S8). This implies that the reduction potential of DsbC-HBx:[2Fe-2S] is fairly negative when compared with canonical [2Fe-2S] clusters (30, 33). In a first experiment we mimicked the conditions employed previously for the bacterial IscU, in which reductive transformation of [2Fe-2S] clusters was afforded by stoichiometric addition of reducing equiv (24). Because the [4Fe-4S] cluster in DsbC-HBx can be reduced to the 1+ state, in contrast to that of IscU that reductively
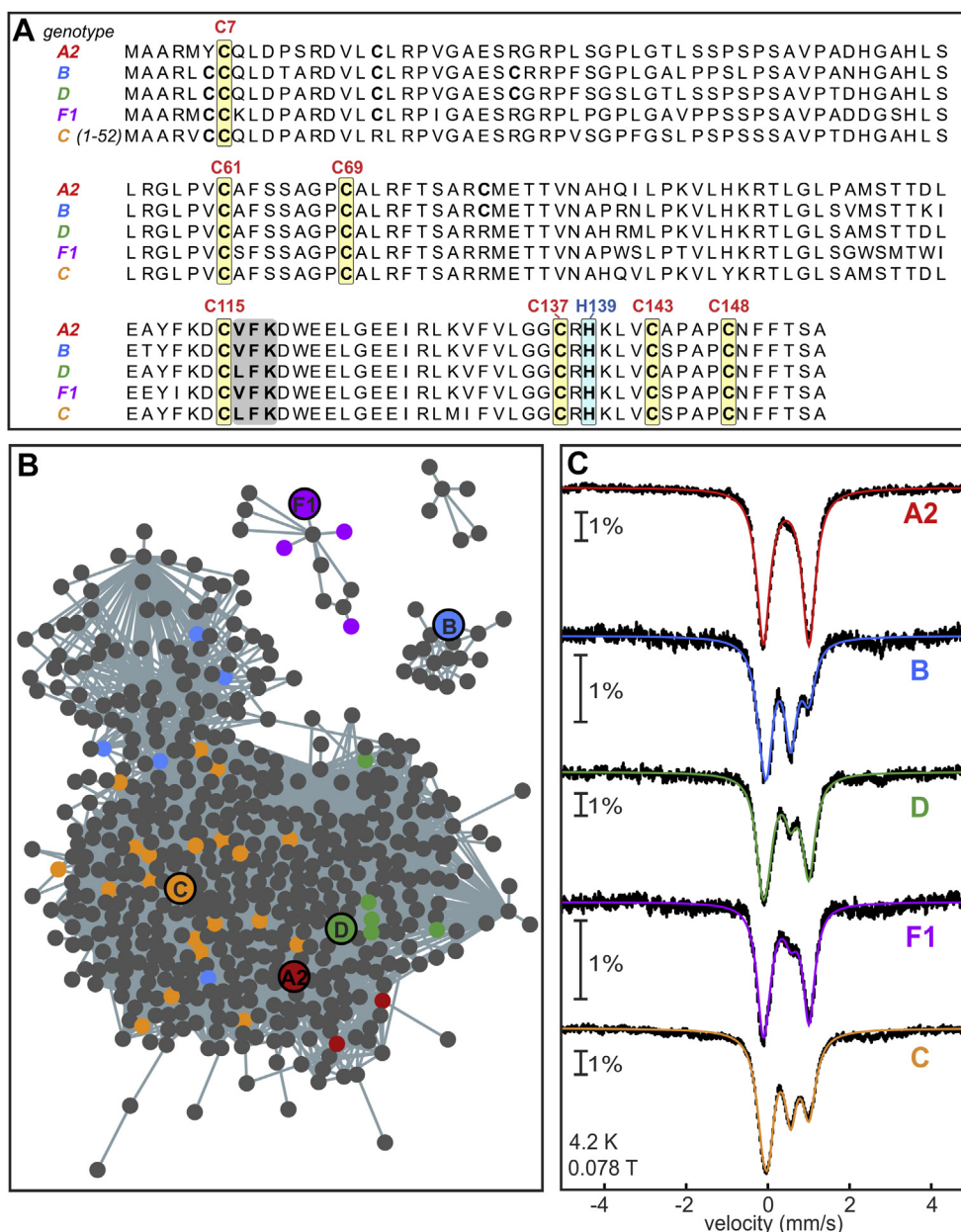
Figure 2. Sequence alignment, Sequence Similarity Network (SSN), and Mössbauer spectra of HBx from select HBV genotypes. *A*, sequence alignment of HBx from HBV genotypes A2, B, C, D, and F1. The N-terminal 52 amino acids of HBx from genotype C have been omitted. The seven strictly conserved cysteines and conserved histidine are highlighted in *yellow* and *blue*, respectively. The LYR-like motif (VFK) is shaded in a *gray box*. *B*, SSN of HBx proteins colored according to their HBV genotype. Nodes (*circles*) include sequences of HBx with ≥95% sequence identity. Edges connect nodes having ≥90.6% sequence identity. *Bold circles* represent the sequences used in this study. Clusters with <4 nodes (240 clusters) were not included in the figure. *C*, Mössbauer spectra of DsbC-HBx from genotypes A2, B, C, D, and F1 isolated anaerobically. Spectra were recorded at 4.2 K with magnetic field (B = 78 mT) applied parallel to the γ-beam. The fits represent the total simulations of the Fe-S content in the sample.

degrades, Mössbauer spectra were recorded at 4.2 and 80 K because spin relaxation for paramagnetic species is temperature dependent (31, 32) (Figs. 4*A* and S7). Upon reaction with 0.7 reducing equiv per protein, DsbC-HBx:[2Fe-2S] exhibits a spectrum that demonstrates loss of 0.35 $[2Fe-2S]^{2+}$ clusters and formation of 0.15 $[4Fe-4S]^{2+}$ clusters per DsbC-HBx (Fig. 4*C*). The nonstoichiometric conversion may be rationalized by loss of reducing equiv toward the one-electron reduction of adventitiously bound Fe^{3+} and $[2Fe-2S]^{2+}$ clusters (the latter verified by EPR by appearance of the axial signal with principal values g_{II} = 2.00, $g_{\perp}$ =1.93) (Fig. 4*D*). Addition of

1.3 reducing equiv leads to an overall loss of 0.65 $[2Fe-2S]^{2+}$ clusters and formation of 0.3 $[4Fe-4S]^{2+/1+}$ clusters per DsbC-HBx. We do not attain the expected 0.35 [4Fe-4S] clusters due to reduction of adventitious Fe^{3+} and further reduction of $[4Fe-4S]^{2+}$ to $[4Fe-4S]^{1+}$ clusters. Reduction with 2.6 reducing equiv affords complete loss of the parent $[2Fe-2S]^{2+}$ centers and formation of 0.5 [4Fe-4S] clusters per DsbC-HBx, 0.4 of which are in the 2+ state, whereas the rest are in the reduced 1+ state. In the whole reductive process, the amount of Fe^{2+} (δ = 1.27 mm/s and ΔE_{Q} = 2.67 mm/s) formed corresponds to the reduction of the initial Fe^{3+} present in the sample,
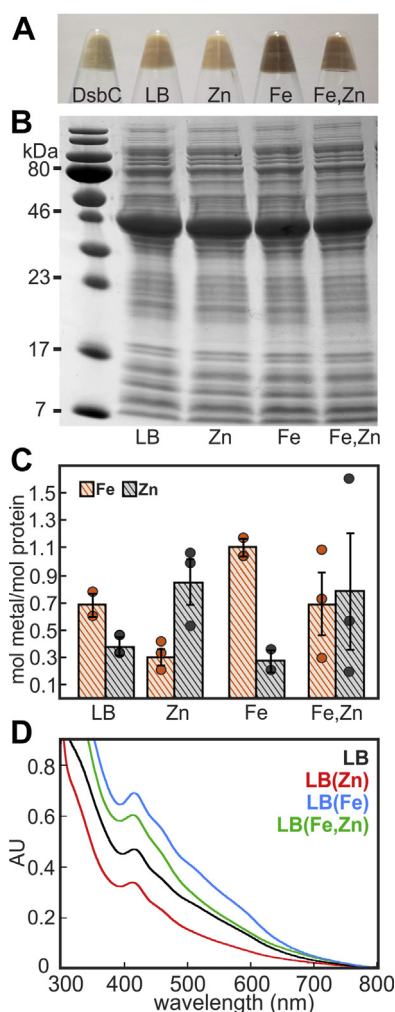
Figure 3. Metal binding properties of DsbC-HBx. *A, E. coli* cell pellets of DsbC-HBx expressed with different metal supplementation, from *left* to *right*: DsbC tag in LB, LB only, LB + 250 μM ZnSO₄, LB + 250 μM Fe(NH₄)₂(SO₄)₂, LB + 250 μM each ZnSO₄ and Fe(NH₄)₂(SO₄)₂. *B,* SDS-PAGE gel of normalized cell pellets, from *left to right*: LB only, LB + 250 μM ZnSO₄, LB + 250 μM Fe(NH₄)₂(SO₄)₂, LB + 250 μM each ZnSO₄ and Fe(NH₄)₂(SO₄)₂. *C,* inductively coupled atomic emission spectrometry analysis of metal content of purified DsbC-HBx expressed under different metal supplementation conditions. *Circles* represent individual data points; error bars represent the standard error of the mean. *D,* UV-visible spectra of purified DsbC-HBx expressed under different metal supplementation conditions.

demonstrating that reductive degradation of Fe-S clusters is negligible (Table S4). Despite the unavoidable consumption of electrons by adventitious free Fe and further reduction of the nascent $[4Fe-4S]^{2+}$ clusters (Fig. 4D), our findings are consistent with a reductive coupling mechanism like that observed for IscU.

Time-dependent reduction

The time-dependent reduction of the [2Fe-2S] to [4Fe-4S] cluster conversion was also monitored by Mössbauer and EPR spectroscopies in an analogous experiment to the one performed for the [Nif]IscA chaperone (35). The starting sample contained 0.8 [2Fe-2S] clusters per protein (Fig. S9) and was reacted with excess sodium dithionite for 1, 5, and 30 min

prior to freezing (Fig. 5A). Already after 1 min, there is a loss of 0.4 $[2Fe-2S]^{2+}$ clusters and formation of 0.2 [4Fe-4S] clusters, while at 5 min 0.65 $[2Fe-2S]^{2+}$ clusters have been reductively consumed and 0.3 $[4Fe-4S]^{2+/1+}$ clusters have been formed. At 30 min, all $[2Fe-2S]^{2+}$ clusters initially present in the sample are reduced, yielding 0.4 $[4Fe-4S]^{2+/1+}$ clusters as a result of reductive coupling and Fe^{2+} stemming mostly from the reduction of adventitious Fe^{3+} in the aerobically isolated sample (Table S5). In parallel EPR time-dependent reduction experiments, the $[2Fe-2S]^{1+}$ state is observed as early as 0.5 min into reduction and maximizes at 5 min, after which the signal decays and completely disappears by 30 min, in agreement with the Mössbauer experiments (Figs. 5B and S9). At 5 min the $[4Fe-4S]^{1+}$ state is detectable, indicating that electrons are concurrently used for reductive coupling and the further reduction of the newly formed $[4Fe-4S]^{2+}$. Collectively, these results are consistent with a reductive coupling scheme in which the $[2Fe-2S]^{1+}$ cluster forms as an intermediate in the production of [4Fe-4S] clusters.

Midpoint potential of the $[4Fe-4S]^{2+/1+}$ redox couple

The 80 K Mössbauer spectrum of the dithionite reduced DsbC-HBx:[4Fe-4S] consists of a major component (90% of the Fe absorption) attributed to both oxidized and reduced [4Fe-4S] clusters and a minor component (10% of the Fe absorption) assigned to high-spin Fe^{2+} (Fig. 6A). Treatment of the $[4Fe-4S]^{2+}$ state with excess dithionite, therefore, does not lead to significant cluster disassembly, unlike the IscU chaperone for which complete cluster decomposition is observed (36). The lack of reductive degradation of the [4Fe-4S] cluster enabled us to measure the midpoint potential of the $[4Fe-4S]^{2+/1+}$ couple by EPR potentiometric titrations on a [4Fe-4S] cluster-enriched sample (Fig. S10). The fraction of $[4Fe-4S]^{1+}$ clusters was followed as a function of the measured potential (Fig. 6B). At the lowest attainable potential (−525 mV), only 55% of the $[4Fe-4S]^{2+}$ clusters present in the sample were reduced to the 1+ state, precluding measurement of the complete titration curve. The estimated midpoint potential (E_m) for the $[4Fe-4S]^{2+/1+}$ couple in HBx is −520 mV (Fig. 6B).

Reversibility of the [2Fe-2S] to [4Fe-4S] cluster conversion

We exposed DsbC-HBx:[4Fe-4S] to molecular O_2 to monitor the extent of [2Fe-2S] cluster formation and other oxidative products by Mössbauer spectroscopy (Fig. 7A). A sample containing 0.5 [4Fe-4S] and 0.1 [2Fe-2S] clusters per protein was first reacted with 1 equiv of O_2 per [4Fe-4S] cluster. The resulting spectrum shows a loss of 0.2 [4Fe-4S] clusters and formation of 0.23 [2Fe-2S] clusters. The rest of the spectral intensity consists of broad paramagnetic signals of high-spin Fe^{3+} stemming from oxidative disassembly of 0.1 [4Fe-4S] clusters. Upon addition of 2 equiv of O_2, there is cumulative loss of 0.26 [4Fe-4S] clusters, gain of 0.3 [2Fe-2S] clusters, and degradation of 0.10 [4Fe-4S] to Fe^{3+}. Oxidative conversion from [4Fe-4S] to [2Fe-2S] clusters is therefore only ∼60% efficient, with a significant fraction of the Fe-S clusters oxidatively degrading to Fe^{3+} (Table S6). The possibility of the
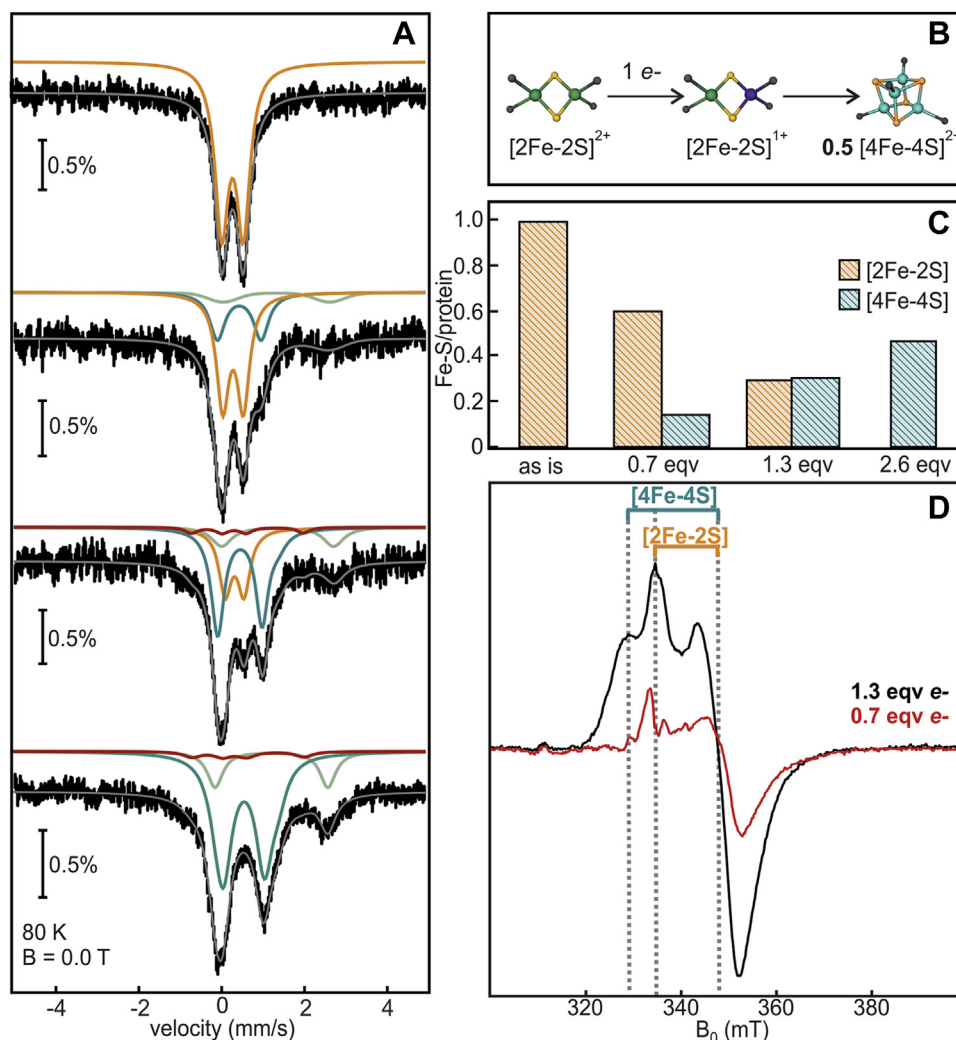
Figure 4. Aerobically isolated DsbC-HBx reacted with stoichiometric reducing equiv. *A*, Mössbauer spectra recorded at 80 K in the absence of an external magnetic field. Spectra from *top* to *bottom*: aerobically isolated, 0.7 reducing equiv, 1.3 reducing equiv, 2.6 reducing equiv. The fits of quadrupole doublet subspectra are shown in *solid lines*: *orange*, $[2Fe\text{-}2S]^{2+}$ clusters; *red*, $[2Fe\text{-}2S]^{1+}$ clusters; *teal*, $[4Fe\text{-}4S]^{1+/2+}$ clusters; *light green*, Fe^{2+}. *B*, scheme of reductive coupling. *C*, graphical representation of the speciation of Fe-S clusters using relative ratios determined from the 80 K Mössbauer spectral fits. *D*, X-band cw EPR spectra of parallel stoichiometric reductions of DsbC-HBx (microwave frequency = 9.38 GHz, T = 10 K, microwave power = 0.64 mW, modulation amplitude = 1 mT). *Gray dotted lines* denote the position of the principal g-values of the Fe-S signals.

small amount of paramagnetic species observed to be assigned to $[3Fe\text{-}4S]^{1+}$ clusters cannot be excluded; however, the resonances are too broad to be consistent with formation of a trinuclear cluster, and also, we have no evidence for accumulation of $[3Fe\text{-}4S]^{1+}$ clusters in the aerobically exposed DsbC-HBx (Figs. 1*B*, S3, and S7). Therefore, we consider the formation of $[3Fe\text{-}4S]^{1+}$ clusters unlikely.

To examine the extent of reversibility of the [2Fe-2S] to [4Fe-4S] transformation, we subjected DsbC-HBx:[2Fe-2S] to consecutive reduction–oxidation cycles while monitoring Fe-S cluster species by UV-visible and EPR spectroscopy. Dithionite reduction of the as-purified DsbC-HBx leads to the disappearance of the $[2Fe\text{-}2S]^{2+}$ cluster optical features (*i.e.*, 415 and 460 nm) and appearance of a single band at 420 nm, consistent with the formation of [4Fe-4S] clusters (Fig. 7*B*). After removing the reductant, the air-exposed sample recovers the $[2Fe\text{-}2S]^{2+}$ cluster optical spectrum, but to a lower extent. The optical features progressively bleach upon multiple rounds of

oxidation and reduction, but cycle between the [2Fe-2S] and [4Fe-4S] cluster forms, showing that they may interconvert multiple times. Cognate EPR experiments were conducted using the $[4Fe\text{-}4S]^{1+}$ state as a quantitative probe of the Fe-S clusters remaining in the sample after each reduction step (Fig. 7*C*). If the first reduction corresponds to the maximal attainable $[4Fe\text{-}4S]^{1+}$ clusters, the signal is reduced to 32% and 11% after the second and third reduction steps, respectively. Overall, these results show that the oxidatively formed [2Fe-2S] clusters can undergo successive rounds of reductive coupling; however, there is significant Fe-S cluster degradation upon each reduction–oxidation cycle (Table S6).

To precisely determine the fate of the Fe-S species during reduction–oxidation, analogous experiments were performed by Mössbauer spectroscopy (Fig. 7*D*). The initial DsbC-HBx:[4Fe-4S] sample consists of 0.3 $[4Fe\text{-}4S]^{2+}$ clusters and 0.25 $[2Fe\text{-}2S]^{2+}$ clusters. This sample was exposed to air for 4 h in the Mössbauer cup and refrozen. The resultant spectrum
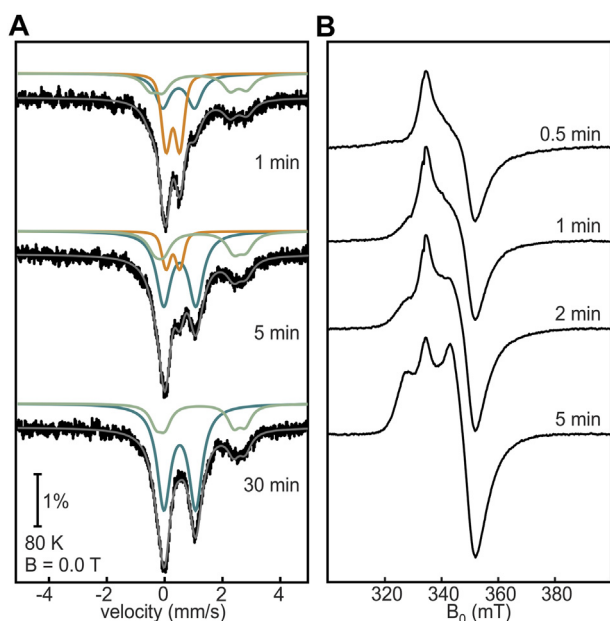
Figure 5. Time-dependent reduction of aerobically isolated DsbC-HBx. *A*, Mössbauer spectra were recorded at 80 K in the absence of an external magnetic field. Total simulations are shown as *gray lines* and are the addition of the subspectra (*orange*, [2Fe-2S]; *teal*, [4Fe-4S]; *light green*, Fe^{2+}). *B*, X-band cw EPR spectra of DsbC-HBx (microwave frequency = 9.38 GHz, T = 10 K, microwave power = 0.64 mW, modulation amplitude = 1 mT).

Figure 6. Reduction of Dsbc-HBx:[4Fe-4S]. *A*, Mössbauer spectrum of anaerobically isolated DsbC-HBx reduced with an excess of sodium dithionite (10 mM) for 30 min recorded at 80 K and in the absence of an external magnetic field. The total simulation (*gray line*) is a sum of two subspectra (*teal*, [4Fe-4S]; *light green*, Fe^{2+}). *B*, redox titration of DsbC-HBx as a function of potential at pH 8.0. The *gray line* corresponds to a fit considering a one-electron transition and was calculated using the Nernst equation.

shows oxidative loss of 0.15 [4Fe-4S] clusters accompanied by an increase of 0.1 [2Fe-2S] clusters. The rest of the Fe appears in mononuclear Fe^{2+} and Fe^{3+}. Rereduction of the oxygen-exposed sample with sodium dithionite results in a spectrum containing 0.4 [4Fe-4S] clusters, demonstrating the reductive coupling of the oxidatively formed [2Fe-2S] clusters. The remaining Fe in the sample (20% of the overall Fe absorption) is assigned to mononuclear Fe^{2+} originating from oxidative cluster disassembly, as estimated by low- and high-temperature spectra (Fig. S11). Considering that there is minimal degradation during the reductive coupling process (Fig. 4), our findings demonstrate that most of the observed Fe-S cluster degradation during oxidation–reduction occurs during the oxidation process.

Discussion

Despite multidecade studies on HBx, little is known about the biophysical and biochemical mechanisms by which HBx affects cellular processes during HBV infection. Here we present evidence that HBx is an Fe-S protein and establish the nuclearity and redox properties of the metallocofactor, providing a framework for future studies and development of therapeutics. HBx binds a [2Fe-2S] or [4Fe-4S] cluster depending on the presence or absence of O_2, respectively, and we have observed that a small amount of [2Fe-2S] clusters is present in whole *E. coli* cells. The [2Fe-2S] cluster appears to be an oxidative outcome, but its persistence in whole cells also suggests an inability of the *E. coli* biosynthetic machinery to insert intact Fe-S clusters. This compromised Fe-S cluster insertion may be alleviated if HBx is overexpressed in
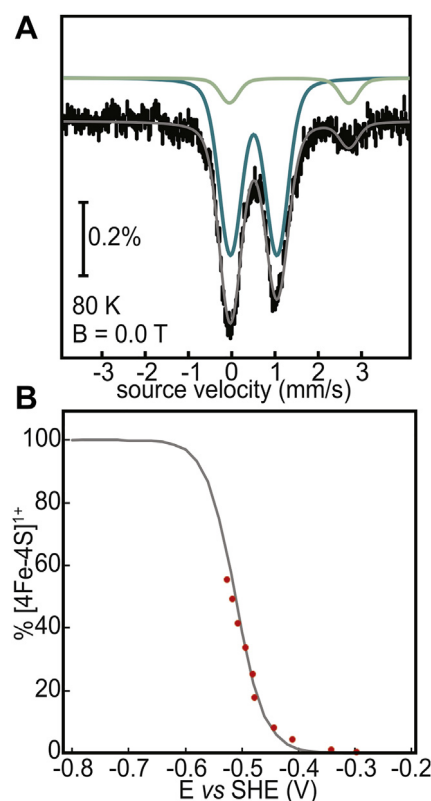
mammalian or insect cells. However, the low solubility of HBx when isolated from insect cells (37) and the variability of HBx overexpression in different mammalian lines pose a significant challenge toward these studies, which nevertheless should be pursued in the near future.

The ability of HBx to coordinate both [2Fe-2S] and [4Fe-4S] clusters is a common feature among sequences from the five HBV genotypes examined (A2, B, C, D, F1), highlighting the potential importance of the Fe-S cofactor in HBx function. HBx is a cysteine-rich polypeptide, offering seven strictly conserved cysteines as likely ligand candidates for the Fe-S cluster. Many of the conserved cysteines have been shown to hold important functional roles, such as C61, C69, and C137, which are crucial for HBx transactivation function (38). We found that single-point cysteine to alanine substitutions allow for wildtype-like Fe-S cluster incorporation and that complete abolition of Fe-S cluster binding is only afforded in a variant lacking all cysteines. Thus, *in vitro* cofactor binding is cysteine dependent but not easily abrogated, suggesting that HBx may reorganize itself to accommodate for Fe-S cluster binding using other available cysteines, protein, or nonprotein residues.

Among the conserved HBx residues, C61, C69, C137, and H139 constitute a CCCH motif reported to coordinate a Zn
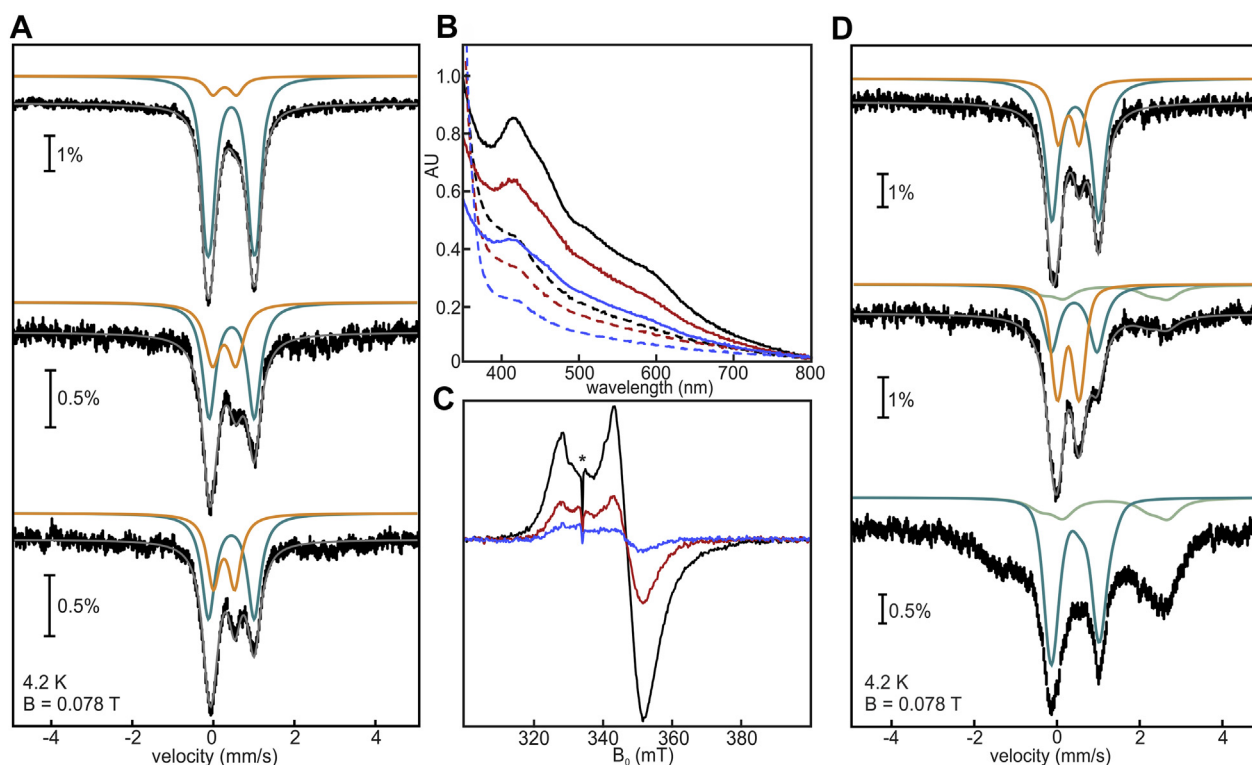
Figure 7. Oxygen exposure and redox cycling of DsbC-HBx. All Mössbauer spectra were recorded at 4.2 K in the presence of a magnetic field (B = 78 mT) applied parallel to the γ-beam. The total simulation (*gray lines*) for all experimental Mössbauer spectra (*vertical bars*) are sums of the fits of the subspectra (*orange*, [2Fe-2S]; *teal*, [4Fe-4S]; *light green*, Fe^{2+}). *A, top,* anaerobically isolated DsbC-HBx, (*middle*) exposed to 1 equiv of O$_2$, (*bottom*) exposed to 2 equiv of O$_2$. *B,* redox cycling monitored by UV-visible spectroscopy. The initial sample (*black solid line*) was reduced with dithionite (*dashed black line*), exposed to air for 1 h (*solid orange line*), reduced again with dithionite (*dashed orange line*), exposed to air for 1 h (*solid blue line*), and finally reduced again with dithionite (*dashed blue line*). *C,* redox cycling monitored by X-band cw EPR spectroscopy (microwave frequency = 9.38 GHz, T = 10 K, microwave power = 0.64 mW, modulation amplitude = 1 mT). The experiment analogous to (*B*) was performed: one reduction (*black*), two rounds of reduction (*orange*), three rounds of reduction (*blue*). *A small sharp signal present in all samples is not Fe-S cluster related and arises from subtraction of a paramagnetic impurity in the resonator. *D, top,* anaerobically isolated DsbC-HBx, (*middle*) exposed to air for 4 h, (*bottom*) rereduced with excess sodium dithionite.

ion (22). The identified CCCH motif was shown to be critical for HBV replication via degradation of the Smc5/6 complex, but a functional role for Zn binding in this respect has not been identified (22). In our study, expression of DsbC-HBx in media with excess Zn results in a decrease in Fe-S cluster enrichment, reflecting competitive ligation of these two co-factors that may occupy the same binding site. Many Fe-S cluster proteins have historically been misidentified as Zn proteins owing to similar ligand requirements (39). The mitochondrial membrane protein mitoNEET was first anno-tated as a Zn-finger protein based on primary sequence but was found to instead bind a [2Fe-2S] cluster (39). The catalytic subunit of RNA polymerase (nsp12) from the severe acute respiratory syndrome coronavirus 2 (SARS-cov-2) was first assigned to be Zn dependent based on cryo-EM structures (29). Subsequent studies revealed that nsp12 harbors instead two [4Fe-4S] clusters, one of which is critical for polymerase activity. Zn has been known to inhibit Fe-S biosynthesis *in vivo* by competitively binding to Fe-S scaffold proteins, including IscU and IscA (40). In biochemical studies and during aerobic purification, Zn can supplant an Fe-S cluster that has been oxidatively degraded, leading to the misassignment of proteins as Zn dependent. In some cases, such as with the SARS-cov-2 nsp12, Zn supports limited protein activity by binding to the

same site as the Fe-S cluster (29) and partially fulfilling a structural role. Thus, from our present data, we cannot exclude that both Zn and the Fe-S cluster may support HBx cellular activity.

The ability of the Fe-S cluster of HBx to transform from a [2Fe-2S] to a [4Fe-4S] cluster under reducing conditions is especially intriguing, since this is a distinctive behavior observed in Fe-S scaffold proteins. Our spectroscopic studies of the DsbC-HBx [2Fe-2S]→[4Fe-4S] transformation are consis-tent with a reductive coupling mechanism that was demon-strated for the bacterial IscU and IscA scaffold proteins (24, 35). This mechanism is thought to be the final step in the *de novo* biosynthesis of [4Fe-4S] clusters, allowing scaffold pro-teins to donate both [2Fe-2S] and [4Fe-4S] clusters to appro-priate acceptor proteins (41). Indirect evidence of reductive coupling is also implied in cluster transfer studies of glutaredoxin-type and other A-type scaffold proteins (*e.g.,* GLRX5, SufA, ISCA1/ISCA2) that require reducing agents to transfer clusters to [4Fe-4S] acceptor proteins (42–45). Reductive coupling in HBx requires the presence of a strong reducing agent, which comes in contrast to A-type scaffolds and glutaredoxins, in which a milder reductant (DTT) can drive the reaction. *A. vinelandii isc*Fdx (E$_m$ = −344 mV) can also serve as the electron donor for reductive coupling in IscU,

but not DsbC-HBx. This observation may not be surprising considering that reduction by ferredoxins is often dependent on protein–protein interactions to facilitate efficient electron transfer (46). The physiological reductant of HBx is presently unknown, but human ferredoxins (*i.e.*, FDX1, FDX2) may serve as better candidates for the reductive coupling in HBx.

There is also some variability in the reversibility of the [2Fe-2S] to [4Fe-4S] conversion among Fe-S scaffold proteins. The majority of [4Fe-4S] clusters in IscU experience O_2-mediated degradation into mononuclear Fe^{3+}, and only a small fraction converts back to [2Fe-2S] clusters (24). In IscA, the process is highly reversible with minimal Fe-S cluster degradation, which can be rationalized considering its proposed role in the maturation of [4Fe-4S] proteins during oxidative stress (35, 47). DsbC-HBx seems to fall in between these two extremes: the Fe-S cluster persists after multiple rounds of oxidation–reduction, albeit with increasing concomitant degradation. Reaction of the reduced Fe-S cluster with O_2 and concomitant release of Fe may act as sources of ROS via Fe-based Fenton chemistry (48). ROS can cause irreversible oxidative damage by nonspecifically reacting with proteins, lipids, and DNA, leading to carcinogenic mutations (49, 50). There is evidence that HBx is associated with an increase in ROS, thereby causing low-level liver inflammation that promotes carcinogenesis (51, 52). In addition, HBx is proposed to associate with the mitochondria and colocalize with membrane proteins such as cytochrome *c* oxidase, which is a major source of ROS generation in the cell (53, 54). Therefore, partial oxidative degradation of the Fe-S cluster in HBx can offer an alternative route by which HBx can modulate mitochondrial reduction potential or protein activities by ROS formation.

The measured reduction potential of the [4Fe-4S]$^{2+/1+}$ transition in DsbC-HBx is appreciably negative (−520 mV), which may argue against this state's physiological relevance. The estimated reduction potential of the [4Fe-4S]$^{2+/1+}$ couple in IscU is similarly low at ∼−570 mV (24). The observed low potential of the IscU [4Fe-4S]$^{2+/1+}$ couple may prevent unwanted electron transfer, which may also be true for HBx. However, at present we cannot rule out the possibility that binding of a partner protein or small molecule may cause a shift to a more positive reduction potential. Taken collectively, our results suggest that the [2Fe-2S]$^{2+}$ and [4Fe-4S]$^{2+}$ forms are likely the relevant cofactor states. The redox behavior of the Fe-S cluster in HBx exhibits similarities to Fe-S donating proteins, suggesting that HBx may be involved in Fe regulation and modulate activity of Fe-S containing proteins, such as the iron regulatory protein 1 (IRP1) (55). The cluster sensitivity to molecular oxygen draws parallels to sensor proteins, such as the oxygen-sensing Fe-S containing transcription factor Fumarate nitrate reductase or the redox-sensitive transcriptional activator SoxR (56, 57). The discovery of an Fe-S cluster in HBx adds to a growing body of work identifying Fe-S clusters in viral proteins and opens new exciting directions to provide insight into the mechanisms that lead to carcinogenic outcomes during chronic HBV infection.

Experimental procedures

Materials

All chemicals were obtained from Fisher Scientific (unless specified otherwise) and were of high purity grade. NCBI accession codes for HBx genotypes: A2, P69713; B, Q8B8Q5; C, Q9YZS7; D, O11883; F1, Q05499.

Expression and isolation of DsbC-HBx

The plasmids encoding MBP-HBx or DsbC-HBx were transformed into Rosetta (DE3) competent cells (New England Biolabs) with the pDB1282 plasmid (kindly gifted by Dr Squire Booker, Pennsylvania State University). Cells were grown in standard Lennox Broth (LB) or M9 minimal media for ^{57}Fe enrichment at 37 °C with shaking (200 rpm) until an A_{600} of ∼0.3 was reached, at which time solid L-Arabinose (0.2% (w/v) final concentration) and solid L-cysteine (200 μM final concentration) were added. At A_{600} of ∼0.7, the cells were cold shocked at 4 °C for 1 h. Protein expression was induced by addition of 0.5 mM isopropyl β-d-1-thiogalactopyranoside (IPTG) and supplemented with 250 μM ^{56}Fe or 125 μM ^{57}Fe. Cells were then incubated at 18 °C for 18 to 20 h and harvested by centrifugation at 7000 rpm for 15 min at 4 °C. Cell pellets were flash frozen in liquid N_2 and stored at −80 °C prior to purification.

Aerobic isolation of DsbC-HBx

DsbC-HBx cell pellets were resuspended in Lysis Buffer (50 mM Hepes, 300 mM NaCl, and 10 mM imidazole, 1 mM TCEP, pH 8.0). Phenylmethylsulfonyl fluoride (PMSF) was added to a final concentration of 45 μg/ml. Cells were broken by sonication, and the clarified lysate was applied onto a gravity Ni-NTA column (McLab) equilibrated in Lysis Buffer. The column was washed with Lysis Buffer, followed by an additional washing with Wash Buffer (50 mM Hepes, 300 mM NaCl, 25 mM imidazole, 1 mM TCEP, pH 8.0). The bound protein was eluted with Elution Buffer (50 mM Hepes, 300 mM NaCl, 250 mM imidazole, 1 mM TCEP, pH 8.0), and fractions containing DsbC-HBx were combined and concentrated using a 30 kDa MWCO Amicon Centrifugal Filter (Millipore, Sigma-Aldrich). The concentrated protein was loaded onto a size exclusion S200 column (GE Healthcare), which was equilibrated with Storage Buffer (50 mM Hepes, 150 mM NaCl, 10% glycerol, pH 8.0). Fractions containing the pure protein were pooled and further concentrated.

Isolation of DsbC-HBx under O₂-free conditions

DsbC-HBx was purified under strictly O_2-free conditions in an anaerobic chamber (Coy Labs) using degassed buffer solutions. DsbC-HBx cell pellets were resuspended in Lysis Buffer, followed by addition of 45 μg/ml PMSF, 0.5 mM ^{57}Fe, 5 mM sodium dithionite, and 2 mM TCEP. Cells were lysed by sonication for a total time of 30 min (15 s pulse, 59 s pause, 60% amplification), during which Na_2S was gradually added to a final concentration of 0.5 mM. The clarified lysate was

applied onto Ni-NTA column equilibrated in Lysis Buffer. The column was washed with Lysis Buffer, followed by an additional washing with Wash Buffer. The bound protein was eluted with Elution Buffer, and fractions containing DsbC-HBx were combined and concentrated using a 30 kDa MWCO Amicon Centrifugal Filter (Millipore, Sigma-Aldrich). Following the purification steps described above, the obtained DsbC-HBx was stored under anaerobic conditions until further use.

Isolation of MBP-HBx

MBP-HBx was purified with a MBPtrap column (5 ml, Cytiva) following the same protocols for DsbC-HBx, apart from small changes in buffer composition: Lysis and Wash Buffer (50 mM Hepes, 300 mM NaCl, 1 mM TCEP, pH 8.0), Elution Buffer (50 mM Hepes, 300 mM NaCl, 10 mM Maltose, 1 mM TCEP, pH 8.0).

Protein and metal quantification

All protein concentrations were determined by the Bradford assay, and protein purity was assessed by SDS-PAGE with Coomassie staining (Thermo Fisher Scientific). Metal analysis of the as-purified proteins was determined by inductively coupled atomic emission spectrometry (ICP-AES). Fe content was determined colorimetrically as described (58).

Sequence similarity network

The SSN was generated with the web-based Enzyme Function Initiative-Enzyme Similarity Tool (EFI-EST) using the Transactivation protein X InterPro family IPR000236 (13,756 sequences) as an input, which was trimmed to contain only full-length HBx (6792 sequences) (59). For the generation of the SSN, an alignment score of 80 was selected, and the final network was further refined by removing edges with a percent sequence identity that was less than 90.6%.

Mössbauer spectroscopy

Mössbauer spectra were recorded on a WEB Research spectrometer equipped with a Janis SVT-400 variable-temperature cryostat. The external magnetic field (0.078 T) was applied parallel to the γ-beam. Zero velocity was calibrated as the centroid of the spectrum of α-Fe recorded at room temperature. WMOSS spectral analysis software (www.wmoss.org, WEB Research) was used to simulate and analyze Mössbauer spectra.

EPR spectroscopy

EPR spectra were recorded on a Bruker E500 Elexsys continuous wave (cw) X-band spectrometer (operating at approximately 9.38 GHz) equipped with a rectangular resonator (TE102) and a continuous-flow cryostat (Oxford 910) with a temperature controller (Oxford ITC 503). All EPR samples were prepared in storage buffer under O_2-free conditions in an anaerobic glovebox (CoyLab). Samples were reduced with excess sodium dithionite for 30 min at 22 °C

prior to being frozen in liquid N_2, unless stated otherwise. Spin concentration was quantified by double integration of signals using 100 μM $CuSO_4$ as a standard.

Stoichiometric and time-dependent reduction of DsbC-HBx

Stock sodium dithionite solutions were prepared fresh prior to every reaction under strictly anaerobic conditions in Storage Buffer and quantified by measuring the absorbance at 315 nm (ε_{315} = 8043 M^{-1} cm^{-1}). For stoichiometric reduction experiments, samples were reacted with sodium dithionite for 30 min at room temperature (∼22 °C) prior to freezing into Mössbauer cups or EPR tubes. For the time-dependent reduction experiments, DsbC-HBx was reacted with excess sodium dithionite (10 mM) at room temperature, and aliquots of the reaction mixture were frozen into Mössbauer cups or EPR tubes at the appropriate timepoints.

Redox titrations monitored by EPR

DsbC-HBx was first enriched in [4Fe-4S] by reducing the aerobically purified protein with excess sodium dithionite (10 mM), which was further removed by a size exclusion HiLoadTM 16/600 Superdex 200 pg column (Cytiva) housed in the anaerobic chamber. For the titration experiment, 4.4 ml of 972.9 μM protein containing 0.61 Fe/protein was maintained under O_2-free conditions in the titration cell by continuous flushing with hydrated argon gas. Reduction or oxidation was afforded by dropwise addition of sodium dithionite or potassium ferricyanide, respectively. The potentials were measured with a pH/redox meter (GPHR 1400, Greisinger) using a combination Pt/Ag/AgCl microelectrode (3 M KCl, Mettler Toledo) and are quoted relative to the standard hydrogen electrode. The electrode was calibrated with a saturated quinhydrone solution at pH 8 (1 M Hepes buffer). The following mediators were added and allowed to equilibrate for 15 min with the protein prior to the actual experiment: 50 μM phenazine methosulfate and 100 μM of the following: 2,6-dichlorophenolindophenol, 1,2-napthoquinone, 1,4-naptho quinone, 5-hydroxy-1,4-napthoquinone, methylene blue, 1,4-dihydroxynapthoquinone, indigo carmine, 2-hydroxyl-1,4-napthoquinone, anthraquinone-1,5-disulfonate, phenosafranine, safranine T, methyl viologen, benzyl viologen. The reduction potential was estimated by simulating the fraction of reduced $[4Fe-4S]^{1+}$ for a one-electron reduction process using the Nernst equation.

Oxygen exposure and redox cycling of DsbC-HBx

For the stoichiometric oxidation experiments, DsbC-HBx:[4Fe-4S] samples were reacted with O_2 by adding appropriate amounts of O_2-saturated Storage Buffer (∼1.8 mM O_2) in a gastight vial for 30 min at room temperature. For time-dependent oxidation, samples were exposed to air at 4 °C before freezing in Mössbauer cups at the respective timepoints. For the redox (reduction–oxidation) cycling, samples were reduced with excess sodium dithionite and exposed to air. Excess dithionite was removed in between

redox cycles with Zeba spin desalting columns (ThermoFisher).

Conflict of interest—The authors declare that they have no conflicts of interest with the contents of this article.

Abbreviations—The abbreviations used are: DDB1, DNA-damage binding protein 1; DsbC, disulfide bond isomerase C; EPR, electron paramagnetic resonance; HBV, hepatitis B virus; ROS, reactive oxygen species; Smc, structural maintenance of chromosomes; SSN, sequence similarity network.

References

1. Zamor, P. J., deLemos, A. S., and Russo, M. W. (2017) Viral hepatitis and hepatocellular carcinoma: Etiology and management. *J. Gastrointest. Oncol.* **8**, 229–242
2. Schweitzer, A., Horn, J., Mikolajczyk, R. T., Krause, G., and Ott, J. J. (2015) Estimations of worldwide prevalence of chronic hepatitis B virus infection: A systematic review of data published between 1965 and 2013. *Lancet* **386**, 1546–1555
3. Velkov, S., Ott, J. J., Protzer, U., and Michler, T. (2018) The global hepatitis B virus genotype distribution approximated from available genotyping data. *Genes (Basel)* **9**, 495
4. Sunbul, M. (2014) Hepatitis B virus genotypes: Global distribution and clinical importance. *World J. Gastroenterol.* **20**, 5427–5434
5. Liang, T. J. (2009) Hepatitis B: The virus and disease. *Hepatology* **49**, S13–S21
6. Kim, C.-M., Koike, K., Saito, I., Miyamura, T., and Jay, G. (1991) HBx gene of hepatitis B virus induces liver cancer in transgenic mice. *Nature* **351**, 317–320
7. Lucifora, J., Arzberger, S., Durantel, D., Belloni, L., Strubin, M., Levrero, M., Zoulim, F., Hantz, O., and Protzer, U. (2011) Hepatitis B virus X protein is essential to initiate and maintain virus replication after infection. *J. Hepatol.* **55**, 996–1003
8. Ng, S. A., and Lee, C. (2011) Hepatitis B virus X gene and hepatocarcinogenesis. *J. Gastroenterol.* **46**, 974–990
9. Decorsiere, A., Mueller, H., van Breugel, P. C., Abdul, F., Gerossier, L., Beran, R. K., Livingston, C. M., Niu, C., Fletcher, S. P., Hantz, O., and Strubin, M. (2016) Hepatitis B virus X protein identifies the Smc5/6 complex as a host restriction factor. *Nature* **531**, 386–389
10. van Breugel, P. C., Robert, E. I., Mueller, H., Decorsiere, A., Zoulim, F., Hantz, O., and Strubin, M. (2012) Hepatitis B virus X protein stimulates gene expression selectively from extrachromosomal DNA templates. *Hepatology* **56**, 2116–2124
11. Saeed, U., Kim, J., Piracha, Z. Z., Kwon, H., Jung, J., Chwae, Y. J., Park, S., Shin, H. J., and Kim, K. (2019) Parvulin 14 and Parvulin 17 bind to HBx and cccDNA and upregulate hepatitis B virus replication from cccDNA to virion in an HBx-dependent manner. *J. Virol.* **93**, e01840-18
12. Bouchard, M. J., and Schneider, R. J. (2004) The enigmatic X gene of hepatitis B virus. *J. Virol.* **78**, 12725–12734
13. Ha, H. L., and Yu, D. Y. (2010) HBx-induced reactive oxygen species activates hepatocellular carcinogenesis via dysregulation of PTEN/Akt pathway. *World J. Gastroenterol.* **16**, 4932–4937
14. Gu, J. M., Lim, S. O., Oh, S. J., Yoon, S. M., Seong, J. K., and Jung, G. (2008) HBx modulates iron regulatory protein 1-mediated iron metabolism via reactive oxygen species. *Virus Res.* **133**, 167–177
15. Geng, M., Xin, X., Bi, L. Q., Zhou, L. T., and Liu, X. H. (2015) Molecular mechanism of hepatitis B virus X protein function in hepatocarcinogenesis. *World J. Gastroenterol.* **21**, 10732–10738
16. Tang, H., Oishi, N., Kaneko, S., and Murakami, S. (2006) Molecular functions and biological roles of hepatitis B virus x protein. *Cancer Sci.* **97**, 977–983
17. Sze, K. M. F., Chu, G. K. Y., Lee, J. M. F., and Ng, I. O. L. (2013) C-terminal truncated hepatitis B virus x protein is associated with metastasis and enhances invasiveness by C-Jun/matrix metalloproteinase protein 10 activation in hepatocellular carcinoma. *Hepatology* **57**, 131–139
18. Zhang, Y., Liu, H., Yi, R., Yan, T., He, Y., Zhao, Y., and Liu, J. (2016) Hepatitis B virus whole-X and X protein play distinct roles in HBV-related hepatocellular carcinoma progression. *J. Exp. Clin. Cancer Res.* **35**, 87
19. de-Medina, T., Haviv, I., Noiman, S., and Shaul, Y. (1994) The X protein of hepatitis B virus has a ribo/deoxy ATPase activity. *Virology* **202**, 401–407
20. Jiang, T., Liu, M., Wu, J., and Shi, Y. (2016) Structural and biochemical analysis of Bcl-2 interaction with the hepatitis B virus protein HBx. *Proc. Natl. Acad. Sci. U. S. A.* **113**, 2074–2079
21. Lee, S. H., Cha, E. J., Lim, J. E., Kwon, S. H., Kim, D. H., Cho, H., and Han, K. H. (2012) Structural characterization of an intrinsically unfolded mini-HBX protein from hepatitis B virus. *Mol. Cells* **34**, 165–169
22. Ramakrishnan, D., Xing, W., Beran, R. K., Chemuru, S., Rohrs, H., Niedziela-Majka, A., Marchand, B., Mehra, U., Zábranský, A., Doležal, M., Hubálek, M., Pichová, I., Gross, M. L., Kwon, H. J., and Fletcher, S. P. (2019) Hepatitis B virus X protein function requires zinc binding. *J. Virol.* **93**, e00250-19
23. Langton, M., and Pandelia, M. E. (2020) Hepatitis B virus oncoprotein HBx is not an ATPase. *ACS Omega* **5**, 16772–16778
24. Chandramouli, K., Unciuleac, M. C., Naik, S., Dean, D. R., Huynh, B. H., and Johnson, M. K. (2007) Formation and properties of [4Fe-4S] clusters on the IscU scaffold protein. *Biochemistry* **46**, 6804–6811
25. Beinert, H., Holm, R. H., and Munck, E. (1997) Iron-sulfur clusters: Nature's modular, multipurpose structures. *Science* **277**, 653–659
26. Rouault, T. (2014) *Iron-Sulfur Clusters in Chemistry and Biology*, De Gruyter, GmbH, Berlin
27. Martin, D., Charpilienne, A., Parent, A., Boussac, A., D'Autreaux, B., Poupon, J., and Poncet, D. (2013) The rotavirus nonstructural protein NSP5 coordinates a [2Fe-2S] iron-sulfur cluster that modulates interaction to RNA. *FASEB J.* **27**, 1074–1083

28. Tsang, S. H., Wang, R., Nakamaru-Ogiso, E., Knight, S. A., Buck, C. B., and You, J. (2016) The oncogenic small tumor antigen of merkel cell polyomavirus is an iron-sulfur cluster protein that enhances viral DNA replication. *J. Virol.* **90**, 1544–1556

29. Maio, N., Lafont, B. A. P., Sil, D., Li, Y., Bollinger, J. M., Jr., Krebs, C., Pierson, T. C., Linehan, W. M., and Rouault, T. A. (2021) Fe-S cofactors in the SARS-CoV-2 RNA-dependent RNA polymerase are potential antiviral targets. *Science* **373**, 236–241

30. Lippard, S. J., and Berg, J. M. (1994) *Principles of Bioinorganic Chemistry*, University Science Books, Sausalito, CA

31. Gütlich, P., Bill, E., and Trautwein, A. X. (2011) *Mössbauer Spectroscopy and Transition Metal Chemistry: Fundamentals and Applications*, Springer-Verlag, Berlin Heidelberg

32. Ueda, C., Langton, M., and Pandelia, M. E. (2021) Characterization of Fe-S clusters in proteins by mössbauer spectroscopy. *Methods Mol. Biol.* **2353**, 281–305

33. Bak, D. W., and Elliott, S. J. (2014) Alternative FeS cluster ligands: Tuning redox potentials and chemistry. *Curr. Opin. Chem. Biol.* **19**, 50–58

34. Maio, N., Singh, A., Uhrigshardt, H., Saxena, N., Tong, W. H., and Rouault, T. A. (2014) Cochaperone binding to LYR motifs confers specificity of iron sulfur cluster delivery. *Cell Metab.* **19**, 445–457

35. Mapolelo, D. T., Zhang, B., Naik, S. G., Huynh, B. H., and Johnson, M. K. (2012) Spectroscopic and functional characterization of iron-sulfur cluster-bound forms of azotobacter vinelandii (Nif)IscA. *Biochemistry* **51**, 8071–8084

36. Agar, J. N., Krebs, C., Frazzon, J., Huynh, B. H., Dean, D. R., and Johnson, M. K. (2000) IscU as a scaffold for iron-sulfur cluster biosynthesis: Sequential assembly of [2Fe-2S] and [4Fe-4S] clusters in IscU. *Biochemistry* **39**, 7856–7862

37. Urban, S., Hildt, E., Eckerskorn, C., Sirma, H., Kekule, A., and Hofschneider, P. H. (1997) Isolation and molecular characterization of hepatitis B virus X-protein from a baculovirus expression system. *Hepatology* **26**, 1045–1053

38. Kumar, V., Jayasuryan, N., and Kumar, R. (1996) A truncated mutant (residues 58-140) of the hepatitis B virus X protein retains transactivation function. *Proc. Natl. Acad. Sci. U. S. A.* **93**, 5647

39. Shimberg, G. D., Pritts, J. D., and Michel, S. L. J. (2018) Iron-sulfur clusters in zinc finger proteins. *Methods Enzymol.* **599**, 101–137

40. Li, J., Ren, X., Fan, B., Huang, Z., Wang, W., Zhou, H., Lou, Z., Ding, H., Lyu, J., and Tan, G. (2019) Zinc toxicity and iron-sulfur cluster biogenesis in Escherichia coli. *Appl. Environ. Microbiol.* **85**, e01967-18

41. Lill, R., and Freibert, S. A. (2020) Mechanisms of mitochondrial iron-sulfur protein biogenesis. *Annu. Rev. Biochem.* **89**, 471–499

42. Beilschmidt, L. K., Ollagnier de Choudens, S., Fournier, M., Sanakis, I., Hograindleur, M. A., Clemancey, M., Blondin, G., Schmucker, S., Eisenmann, A., Weiss, A., Koebel, P., Messaddeq, N., Puccio, H., and Martelli, A. (2017) ISCA1 is essential for mitochondrial Fe4S4 biogenesis *in vivo*. *Nat. Commun.* **8**, 15124

43. Nasta, V., Suraci, D., Gourdoupis, S., Ciofi-Baffoni, S., and Banci, L. (2020) A pathway for assembling [4Fe-4S](2+) clusters in mitochondrial iron-sulfur protein biogenesis. *FEBS J.* **287**, 2312–2327

44. Gupta, V., Sendra, M., Naik, S. G., Chahal, H. K., Huynh, B. H., Outten, F. W., Fontecave, M., and Ollagnier de Choudens, S. (2009) Native Escherichia coli SufA, coexpressed with SufBCDSE, purifies as a [2Fe-2S]

45. Brancaccio, D., Gallo, A., Mikolajczyk, M., Zovo, K., Palumaa, P., Novellino, E., Piccioli, M., Ciofi-Baffoni, S., and Banci, L. (2014) Formation of [4Fe-4S] clusters in the mitochondrial iron-sulfur cluster assembly machinery. *J. Am. Chem. Soc.* **136**, 16240–16250

46. Weiler, B. D., Bruck, M. C., Kothe, I., Bill, E., Lill, R., and Muhlenhoff, U. (2020) Mitochondrial [4Fe-4S] protein assembly involves reductive [2Fe-2S] cluster fusion on ISCA1-ISCA2 by electron flow from ferredoxin FDX2. *Proc. Natl. Acad. Sci. U. S. A.* **117**, 20555–20565

47. Blanc, B., Gerez, C., and Ollagnier de Choudens, S. (2015) Assembly of Fe/S proteins in bacterial systems: Biochemistry of the bacterial ISC system. *Biochim. Biophys. Acta* **1853**, 1436–1447

48. Wardman, P., and Candeias, L. P. (1996) Fenton chemistry: An introduction. *Radiat. Res.* **145**, 523–531

49. Qian, S. Y., and Buettner, G. R. (1999) Iron and dioxygen chemistry is an important route to initiation of biological free radical oxidations: An electron paramagnetic resonance spin trapping study. *Free Radic. Biol. Med.* **26**, 1447–1456

50. Toyokuni, S. (2009) Role of iron in carcinogenesis: Cancer as a ferrotoxic disease. *Cancer Sci.* **100**, 9–16

51. Ling, L. R., Zheng, D. H., Zhang, Z. Y., Xie, W. H., Huang, Y. H., Chen, Z. X., Wang, X. Z., and Li, D. (2020) Effect of HBx on inflammation and mitochondrial oxidative stress in mouse hepatocytes. *Oncol. Lett.* **19**, 2861–2869

52. Lim, W., Kwon, S. H., Cho, H., Kim, S., Lee, S., Ryu, W. S., and Cho, H. (2010) HBx targeting to mitochondria and ROS generation are necessary but insufficient for HBV-induced cyclooxygenase-2 expression. *J. Mol. Med. (Berl.)* **88**, 359–369

53. Li, D., Ding, J., Chen, Z., Chen, Y., Lin, N., Chen, F., and Wang, X. (2015) Accurately mapping the location of the binding site for the interaction between hepatitis B virus X protein and cytochrome c oxidase III. *Int. J. Mol. Med.* **35**, 319–324

54. Zheng, B. Y., Fang, X. F., Zou, L. Y., Huang, Y. H., Chen, Z. X., Li, D., Zhou, L. Y., Chen, H., and Wang, X. Z. (2014) The co-localization of HBx and COXIII upregulates COX-2 promoting HepG2 cell growth. *Int. J. Oncol.* **45**, 1143–1150

55. Funauchi, Y., Tanikawa, C., Yi Lo, P. H., Mori, J., Daigo, Y., Takano, A., Miyagi, Y., Okawa, A., Nakamura, Y., and Matsuda, K. (2015) Regulation of iron homeostasis by the p53-ISCU pathway. *Sci. Rep.* **5**, 16497

56. Khoroshilova, N., Popescu, C., Munck, E., Beinert, H., and Kiley, P. J. (1997) Iron-sulfur cluster disassembly in the FNR protein of Escherichia coli by O2: [4Fe-4S] to [2Fe-2S] conversion with loss of biological activity. *Proc. Natl. Acad. Sci. U. S. A.* **94**, 6087–6092

57. Hidalgo, E., Bollinger, J. M., Jr., Bradley, T. M., Walsh, C. T., and Demple, B. (1995) Binuclear [2Fe-2S] clusters in the Escherichia coli SoxR protein and role of the metal centers in transcription. *J. Biol. Chem.* **270**, 20908–20914

58. Stookey, L. L. (1970) Ferrozine—a new spectrophotometric reagent for iron. *Anal. Chem.* **42**, 779–781

59. Gerlt, J. A., Bouvier, J. T., Davidson, D. B., Imker, H. J., Sadkhin, B., Slater, D. R., and Whalen, K. L. (2015) Enzyme function initiative-enzyme similarity tool (EFI-EST): A web tool for generating protein sequence similarity networks. *Biochim. Biophys. Acta* **1854**, 1019–1037